

Deep Learning Model-based Decision Support System for Kidney Cancer on Renal Images

Mohamed Tounsi

College of Computer and Information Sciences, Prince Sultan University, Riyadh, Saudi Arabia | Automated Systems and Soft Computing Lab (ASSCL), Prince Sultan University, Riyadh, Saudi Arabia | mtounsi@psu.edu.sa

Donya Y. Abdulhussain

Department of Cybersecurity and Cloud Computing Technical Engineering, Uruk University, Baghdad, Iraq | donya_yasir@uruk.edu.iq

Ahmad Taher Azar

College of Computer and Information Sciences, Prince Sultan University, Riyadh, Saudi Arabia | Automated Systems and Soft Computing Lab (ASSCL), Prince Sultan University, Riyadh, Saudi Arabia | Faculty of Computers and Artificial Intelligence, Benha University, Egypt | aazar@psu.edu.sa, ahmad.azar@fci.bu.edu.eg

Ahmed Al-Khayyat

College of Technical Engineering, The Islamic University, Najaf, Iraq | College of Technical Engineering, The Islamic University of Al Diwaniyah, Iraq | College of Technical Engineering, The Islamic University of Babylon, Iraq | ahmedalkhayyat85@gmail.com

Ibraheem Kasim Ibraheem

Department of Electrical Engineering, College of Engineering, University of Baghdad, Iraq | ibraheemki@coeng.uobaghdad.edu.iq (corresponding author)

Received: 8 July 2024 | Revised: 7 August 2024 | Accepted: 11 August 2024

Licensed under a CC-BY 4.0 license | Copyright (c) by the authors | DOI: <https://doi.org/10.48084/etasr.8335>

ABSTRACT

Kidney cancer comes in various forms. Renal Cell Carcinoma (RCC) is the most severe and common kind of kidney cancer. Earlier diagnosis of kidney cancer has enormous advantages in implementing preventive measures to reduce its effects and death rates and overcome the tumor. Manually detecting Whole Slide Images (WSI) of renal tissues is a basic approach to predicting and diagnosing RCC. However, manual analysis of RCC is prone to inter-subject variability and is time-consuming. Compared to time-consuming and tedious classical diagnostic methods, automatic Deep Learning (DL) detection algorithms can improve test accuracy and reduce diagnostic time, radiologist workload, and costs. The study presents a Computational Intelligence with a Deep Learning Decision Support System for Kidney Cancer (CIDL-DSSKC) technique on renal images. The CIDL-DSSKC model analyzes renal images to identify and classify kidney cancer. The proposed method uses Median and Wiener filters for image preprocessing and the Xception model to derive a useful set of feature vectors. In addition, the Flower Pollination Algorithm (FPA) is employed to optimally choose parameters for the Xception method. The β -Variational Autoencoder (β -VAE) approach is employed for the identification and classification of kidney cancer. The proposed model was used in a renal image dataset that contained many images, achieving more than 98% accuracy and 97% precision, recall, and F score.

Keywords-computational intelligence; nature-inspired algorithm; deep learning; decision support system; kidney cancer

I. INTRODUCTION

Kidney cancer occurs mainly in men than in women [1]. Renal Cell Carcinoma (RCC) is an aggressive and common kind of kidney cancer in patients, especially adults. Annually, approximately 300,000 people are affected around the world, and it is responsible for more than 100,000 deaths [2]. RCCs grow in the lining of the proximal kidney tubule, whereas tumor cells grow over time and can be deployed over other organs. Usually, the symptoms of RCC are hidden and not easily diagnosed. Numerous problems obstruct the classification of RCC subtypes, such as the lack of an enormous dataset with accurately localized annotations [3]. In addition, there is a simple data imbalance because clear cell subtypes include variations in the appearance of similar subtypes at multiple resolution levels in most medical cases and the coherence of RCC cells in various subtypes is also challenging [4]. Current RCC classification frameworks depend on valuable annotations of pathology digital images [5].

Various computational methods have been proposed to address such challenges in analyzing HPI for diagnostic purposes in multiple tumors [6]. This analysis has been based conventionally on applying classification algorithms that process handcrafted image-derived features, such as cell shape, pixel, and size intensity distribution, monitored in selected image patches or full images [7]. With the increasing volume of histology datasets and the wide acceptance of whole-image high-content imaging, Deep Learning (DL) approaches can be applied [8-11]. Unlike the previous generation of Machine Learning (ML) techniques, DL approaches are based on Convolutional Neural Networks (CNNs) processing raw intensity images and automatically learning to extract prediction features [12-16]. The potential and accuracy of DL models in analyzing HPI for prognostic and diagnostic purposes have been exposed in many research fields [17]. Therefore, DL could play a prominent role in the era of precision medicine and digital pathology.

This study proposes a Computational Intelligence with a Deep Learning Decision Support System for Kidney Cancer (CIDL-DSSKC) detection on renal histopathology images. The proposed CIDL-DSSKC uses median and Wiener filters for image preprocessing and the Xception model to derive a useful set of feature vectors. In addition, the Flower Pollination Algorithm (FPA) is leveraged to choose parameters for the Xception method. The β -Variational Autoencoder (β -VAE) approach is employed to detect and recognize kidney cancer.

II. RELATED WORKS

In [18], a DL technique was proposed that mechanically divided the complicated nuclei in histological images, applying a potential encoding and decoding structure with an SCPP-Net separable convolutional pyramid-pooling network. The SCPP unit focused on two main characteristics: at first, it raised the receptive domain by changing four dilation rates, kept the kernel size set, and then reduced trained parameters through depthwise convolution. In [19], a method was introduced to inspect the impact of Transfer Learning (TL) on Computed Tomography (CT) scans in detecting malignant and benign renal cancers. This study also introduced patient-level

approaches to enhance classification accuracy. The InceptionV3 model, pre-trained on the ImageNet dataset, was cross-trained for the classification task. In [20], a DNN method was presented to precisely classify digitized biopsy and surgical resection images into five classes: chromophobe RCC, clear cell RCC, renal oncocyoma, and papillary RCC.

In [21], a new DL structure was devised and evaluated in discriminating papillary and clear cell RCCs. This DL structure consisted of 3 CNNs. Whole-slide kidney images were classified as patches with three sizes, whereas all networks processed particular patch sizes. In [22], a multimodal DL model (MMDLM) was proposed for ccRCC diagnosis. In [23], an end-to-end DL method was presented to diagnose the five most important histological subtypes of renal cancers, including both malignant and benign cancers in multiphase CTs. In [24], a new structure (Kidney-SegNet) was developed, combining the efficacy of related encoder and decoder structures with spatial pyramid pooling and including effective dimension-wise convolutions. In [25], a new DL-based technique was proposed to enhance the computation efficacy of histological image classification. This approach worked at both the slide and the tissue level, eliminating the need for complex patch-level labeling.

III. MATERIALS AND METHODS

This study presents the CIDL-DSSKC to identify and detect kidney cancer in renal images. This approach encompasses many subprocesses, such as image preprocessing, Xception feature selection, FPA-based parameter tuning, and β -VAE based classification. Figure 1 demonstrates the entire flow of CIDL-DSSKC.

A. Data Used

The CIDL-DSSKC was tested in the CT Kidney dataset [26], which contains 4000 samples in four classes.

B. Image Preprocessing

Image preprocessing was carried out to optimize image quality. In general, degraded images, prone to noise, are restored by proper techniques such as filtering [27].

$$g(x, y) = f(x, y) * u(x, y) + n(x, y) \quad (1)$$

$$h(x, y) = R[g(x, y)] \quad (2)$$

where $g(x, y)$ indicates the output degraded image, $u(x, y)$ denotes the degradation function, $f(x, y)$ refers to the acquired image, $*$ shows the convolution, $n(x, y)$ signifies noise, namely Gaussian noise, and $h(x, y)$ denotes the concluding output image. The degraded image was inputted into the noise reduction filters, namely the Median (MF) and Wiener (WF) filters, to obtain denoised gamma images. A noise reduction filter with a nonlinear spatial domain is frequently applied to obtain denoised images.

The procedure to improve image quality is given in the following: At first, the mask matrix of $n \times m$ size is fixed for the reduction of spatial noise. In contrast to the mask pixel value for the noisy images, respective to the mask pixel dimensions, the mask matrix is used to recalculate the newest pixel value. The median filter modifies all the pixel values to

the median pixel value respectively to the mask matrix at the central pixel value. The WF includes the average pixel and variance values in the $n \times m$ size, and is given as follows:

$$m = \frac{1}{NM} \sum_{n,m \in \eta} a(n, m) \quad (3)$$

$$\sigma^2 = \frac{1}{NM} \sum_{n,m \in \eta} a^2(n, m) - \mu^2 \quad (4)$$

where $a(n, m)$ represents all the pixels in the area η , μ indicates the mean, σ^2 denotes the variance of Gaussian noise,

and $n \times m$ denotes the size of the neighborhood region η in the mask. The WF is expressed to the newest pixel that is characterized by $b_w(n, m)$ using the estimated value

$$b_w(n, m) = \mu + \frac{\sigma^2 - v^2}{\sigma^2} \cdot (a(n, m) - \mu) \quad (5)$$

where v^2 denotes the noise variance setting of the mask matrix for the WF applications.

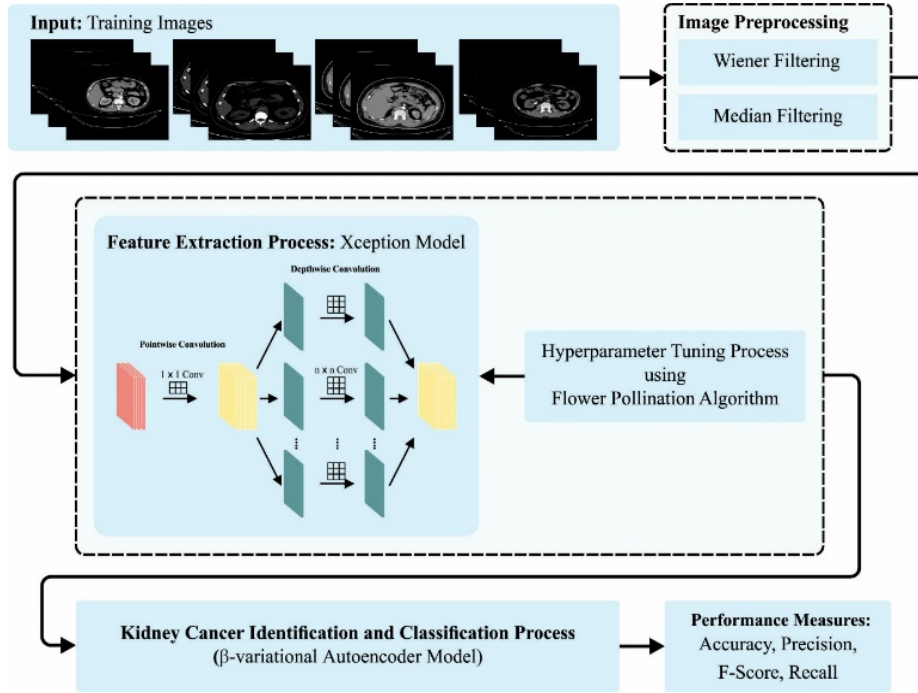


Fig. 1. The overall flow of the CIDL-DSSKC method.

C. Feature Extraction: Optimal Xception Model

The Xception model is used to produce effectual feature vectors. Xception, an amended version of InceptionV3, is a depthwise separable convolution (Conv) based DNN model [28]. All input streams are processed utilizing one convolution filter during a Conv procedure called depthwise Conv. A kind of Conv, named pointwise Conv, exploits a 1×1 kernel that repeats over all points. The kernel depth corresponds to the number of channels in the source images. A pointwise Conv was merged with depthwise Conv to generate a depthwise Conv layer.

After the depthwise Conv, pointwise Conv takes place in the original depthwise separable Conv layer, and then, a depthwise Conv layer takes place in the improved depthwise Conv. The Xception module utilizes an adapted separable Conv. The separable Conv is the modified depthwise separable Conv with a remaining connection from the middle flow. The data passes through the input flow, then through the middle flow, and finally through the exit flow. Average pooling with 4×4 size and dense and flattening layers are added to classify the image.

This study uses FPA to choose the parameters of the Xception approach, which is based on the pollination behavior of flowering plants [29]. The key points of this technique are:

- Concept 1: Local search (local pollination) can be described by the abiotic and self-pollination in wildlife.
- Concept 2: Global search (global pollination) is represented by biotic and cross-pollination, which depends on Lévy flight.
- Concept 3: The reproduction probability assumes that the potential solution (flower stability) is equivalent to the similarity of the two flowers.
- Concept 4: Global and local pollination can be affected by any external reason. Thus, the balance among global and local pollinations can be controlled by the switching probability $p \in [0, 1]$.

Consider a search space $\mathcal{Y} = \{s_1, s_2, \dots, s_m\}$ of potential solutions so that $s_i \in \mathbb{R}^n$ FPA to resolve the subsequent challenges:

$$s^* = \operatorname{argmin}_{s \in \mathcal{Y}} \{f(s)\} \quad (6)$$

where $f(\cdot)$ refers to the objective function. In general, the FPA working process consists of 5 stages, as follows.

1) Step 1: Parameter Description

FPA includes subsequent parameters:

- m implies the population size (count of flowers or solutions).
- s_{best} signifies the present optimum solution.
- l shows the size of the step.
- p denotes the switching probability that resolves if global or local pollination is subsequently FPA.

2) Step 2: Population Initialization

Initialize the decision variable $x \in \mathfrak{x}$ in the random range. One method \mathfrak{x} is represented as a bi -dimension matrix, $\mathfrak{x} \in \mathfrak{R}^{m \times n}$:

$$FPX = \begin{bmatrix} x_1^1 & x_2^1 & \dots & x_n^1 \\ x_1^2 & x_2^2 & \dots & x_n^2 \\ \vdots & \vdots & \dots & \vdots \\ x_1^m & x_2^m & \dots & x_n^m \end{bmatrix} \quad (7)$$

where $x_{i,j} \in [l_j, u_j]$ so that l_j and u_j refer to the lower and upper bounds of the j^{th} search space, correspondingly. Each potential solution (flower) is initialized using

$$x_{i,j} = l_j + (u_j - l_j) \times q \quad (8)$$

where q represents a scalar random number within $[0,1]$. Based on the FF value, the generated solution is stored in \mathfrak{x} in ascending sequence $(x_1) \leq f(x_2) \leq \dots \leq f(x_m)$. In addition, the global optimum flower s_{best} is initialized by $s_{best} = x_1$.

3) Step3: Present Flower Population Intensification

As mentioned, p determines whether the pollinator follows global or local pollination.

- Local Search (Abiotic): this pollination occurs without a pollinator, thus the broadcast of pollen relies on the wind and diffusion. The local pollination and flower constancy at r time step is characterized by

$$s_i^{t+1} = s_i^t + \varepsilon(s_j^t - s_c^t) \quad (9)$$

The basis is to mimic the constancy of flowers from the local neighborhood. According to statistical data, s_j^t and s_k^t either come from identical species or are selected from the FPA population.

- Global Search (Biotic): the pollen of flowers can be transferred long-distance via pollinators such as bees, bats, birds, and so on. This ensures that reproduction and pollination are the most suitable. The biotic FPA procedure can be represented as

$$x_i^{t+1} = x_i^t + L(x_{best} - x_i^t) \quad (10)$$

For insects that travel long distances with dissimilar step sizes, Lévy flight can be used to effectively imitate their

characteristics. Thus, the representation of $L > 0$ from the Levy distribution is expressed as

$$L \sim \frac{\lambda \Gamma(\lambda) \sin(\frac{\pi\lambda}{2})}{\pi} \frac{1}{Q^{1+\lambda}} \quad (11)$$

where $\Gamma(\lambda)$ represents the gamma function that has larger steps ($Q^n s_0 > 0$). Here, λ is fixed at 1.5.

4) Step 4: FPA Upgrading with Global Optimum Flower

The optimum flower s_{best} is upgraded for all the iterations t if $f(s_i^t) < f(s_{best})$, $\forall i = 1, 2, \dots, m$.

5) Step 5: Stopping condition.

FPA iterates steps 3 and 4 until the ending criteria, the iteration number or the quality of the result, are satisfied. Fitness choice is a main problem. An encoder result is used to estimate the best solution candidate. Here, the exactness value is a major state applied to FF

$$Fitness = \max(P) \quad (12)$$

$$P = \frac{TP}{TP+FP} \quad (13)$$

where TP and FP imply true and false positive values, respectively.

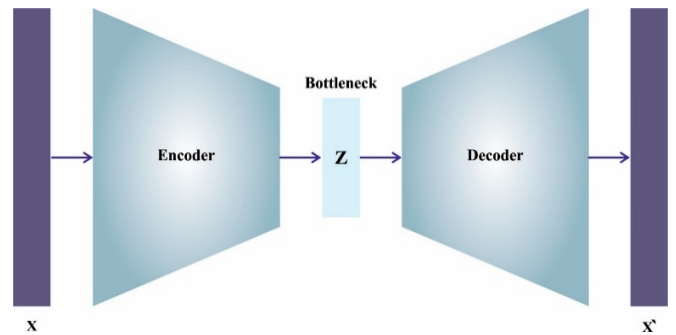


Fig. 2. Structure of VAE.

D. Image Classification: β -VAE Model

Finally, the classification of kidney cancer takes place utilizing the β -VAE method. VAE is a generative mechanism that comprises encoding and decoding parts, aiming to increase the marginal probability of the reconstruction output as [30-33]

$$\log_{p_\theta}(X) \geq E_{z \sim q_\phi(Z|X)}[\log_{p_\theta}(X|Z)] -$$

$$D_{KL}(q_\phi(Z|X) || p(Z)) \quad (14)$$

Here, the initial period is the log probability that input X produced by the sampled Z in the inferred distribution $q_\phi(Z|X)$. This distribution is considered to follow the multivariate standard distribution. Figure 2 illustrates the VAE substructure.

The loss function of VAE comprises a first term that finds the reconstructed error among the inputs and outputs and a second one that forces the learned distribution $q_\phi(Z|X)$ to be the same for the prior distribution $p(Z)$.

$$\mathcal{L}_{VAE(\theta, \varphi)} = \mathcal{L}_{recon}(\theta, \varphi) + \mathcal{L}_{KL}(\theta, \varphi) \quad (15)$$

The reconstruction loss $\mathcal{L}_{recon}(\theta, (\theta, \varphi))$ and the KL loss $\mathcal{L}_{KL}(\theta, (\theta, \varphi))$ are evaluated using

$$\mathcal{L}_{recon}(\theta, (\theta, \varphi)) = \sum_{i=1}^N \|\hat{X} - X\|_2^2 \quad (16)$$

$$\mathcal{L}_{KL}(\theta, (\theta, \varphi)) = D_{KL}(q_{\varphi})(Z|X) \| p(Z) \quad (17)$$

β -VAE has demonstrated good performance using multiple disentanglement metrics. This model uses it as a backbone to encourage disentanglement. β -VAE is an extension of typical VAE that aims to acquire the disentangled representation of the encoder variable in an unsupervised way by providing additional weight to the KL term than the original VAE, using an extra hyperparameter β .

$$\mathcal{L}_{VAE}(\theta, \varphi) = \mathcal{L}_{recon}(\theta, \varphi) + \beta \mathcal{L}_{KL}(\theta, \varphi) \quad (18)$$

IV. RESULTS AND DISCUSSION

The effectiveness of the proposed CIDL-DSSKC method was examined on the CT dataset [26], which consists of 4000 instances with four class labels, as shown in Table I.

TABLE I. DATASET DETAILS [26]

Classes	No. of samples
Normal	1000
Cyst	1000
Tumor	1000
Stone	1000
Total	4000

Figure 3 shows the confusion matrices of CIDL-DSSKC. The results show that the CIDL-DSSKC technique identifies the four classes competently. Table II and Figure 4 show the results of the CIDL-DSSKC method for an 80:20 Training (TRPH)/Testing (TSPH) split. The experimental results indicate that the CIDL-DSSKC model attained satisfactory results. On 80% TRPH, the CIDL-DSSKC model achieved average $accu_y$, $prec_n$, $reca_l$, and F_{score} of 98.33%, 96.65%, 96.66%, and 96.65%, respectively. On 20% of TRPH, the CIDL-DSSKC method achieved average $accu_y$, $prec_n$, $reca_l$, and F_{score} of 97.81%, 95.61%, 95.54%, and 95.56%, respectively.

Figure 5 shows the $accu_y$ value of the CIDL-DSSKC technique during the training and validation in 80:20 TRPH/TSPH. The CIDL-DSSKC obtains the highest $accu_y$ values over increasing epochs. Also, the maximum validation $accu_y$ over its training value shows that the CIDL-DSSKC method learns efficiently in 80:20 TRPH/TSPH. Figure 6 shows a brief precision/recall analysis of the proposed method, showing that it can achieve great precision/recall values on all class labels. Figure 7 shows the ROC curve of the CIDL-DSSKC model for 80:20 TRPH/TSPH, demonstrating enhanced ROC values across all classes.

TABLE II. RESULTS ON 80:20 TRPH/TSPH

Classes	$Accu_y$	$Prec_n$	$Reca_l$	F_{score}
Training Phase (80%)				
Normal	99.19	98.12	98.61	98.37
Cyst	97.38	95.64	93.71	94.66
Tumor	97.78	95.57	95.69	95.63
Stone	98.97	97.28	98.62	97.95
Average	98.33	96.65	96.66	96.65
Testing Phase (20%)				
Normal	99.38	98.55	99.03	98.79
Cyst	96.37	91.90	94.15	93.01
Tumor	96.50	93.96	90.96	92.43
Stone	99.00	98.01	98.01	98.01
Average	97.81	95.61	95.54	95.56

Table III and Figure 8 show the detection results of the CIDL-DSSKC for a 70:30 TRPH/TSPH split. In 70% TRPH, the CIDL-DSSKC method achieved average $accu_y$, $prec_n$, $reca_l$, and F_{score} of 98.41%, 96.85%, 96.82%, and 96.83%, respectively. In 30% TRPH, the CIDL-DSSKC system attained average $accu_y$, $prec_n$, $reca_l$, and F_{score} of 98.87%, 97.73%, 97.73%, and 97.73%, respectively. Figure 9 shows the $accu_y$ results of the CIDL-DSSKC model at the training and validation process in a 70:30 TRPH/TSPH split. These results indicate that the CIDL-DSSKC method achieved higher $accu_y$ values over increasing epochs. Also, the maximum validation $accu_y$ over the respective training values indicates that the CIDL-DSSKC learns efficiently at a 70:30 TRPH/TSPH split.

TABLE III. RESULTS ON 70:30 TRPH/TSPH

Classes	$Accu_y$	$Prec_n$	$Reca_l$	F_{score}
Training Phase (70%)				
Normal	99.29	98.54	98.54	98.54
Cyst	97.68	95.12	95.79	95.45
Tumour	98.50	96.56	97.63	97.09
Stone	98.18	97.17	95.32	96.24
Average	98.41	96.85	96.82	96.83
Testing Phase (30%)				
Normal	99.58	99.05	99.36	99.21
Cyst	98.33	96.21	96.88	96.54
Tumor	99.00	98.21	97.52	97.86
Stone	98.58	97.46	97.15	97.31
Average	98.87	97.73	97.73	97.73

Figure 10 shows the loss analysis of the CIDL-DSSKC at training and validation in a 70:30 TRPH/TSPH split, indicating that it achieves close values of training and validation loss. The proposed CIDL-DSSKC learns effectively in this TRPH/TSPH split. Figure 11 shows a precision/recall curve of the proposed method in 70:30 TRPH/TSPH, indicating that it attains great precision/recall values in all classes. Figure 12 shows a ROC analysis of the CIDL-DSSKC method in 70:30 TRPH/TSPH, indicating superior ROC values across all classes.

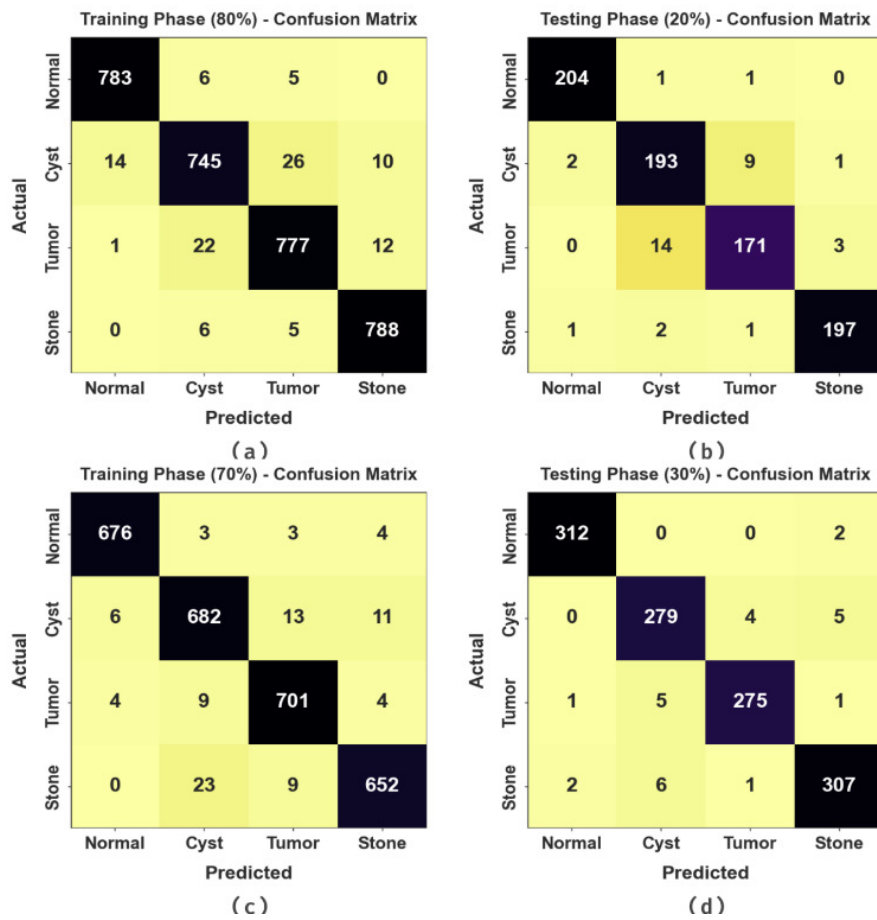


Fig. 3. Confusion matrices of the CIDL-DSSKC method: (a, b) 80:20 TRPH/TSPH, and (c,d) 70:30 TRPH/TSPH

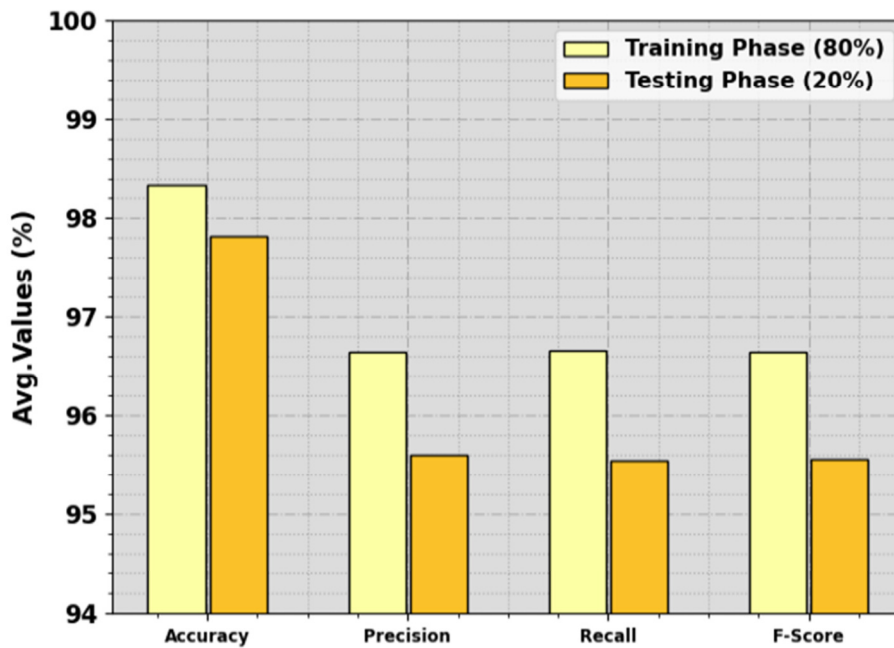


Fig. 4. Average results of CIDL-DSSKC in 80:20 TRPH/TSPH.



Fig. 5. CIDL-DSSKC accuracy in 80:20 TRPH/TSPH split.

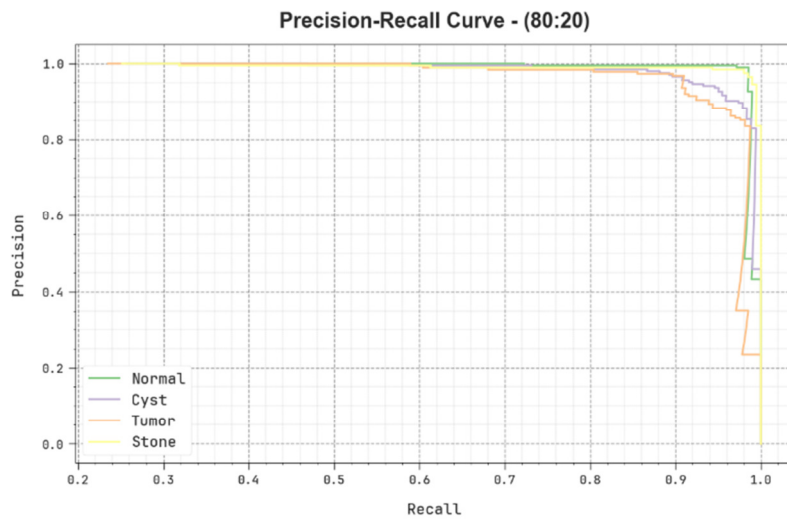


Fig. 6. Precision/Recall curve of CIDL-DSSKC in 80:20 TRPH/TSPH.

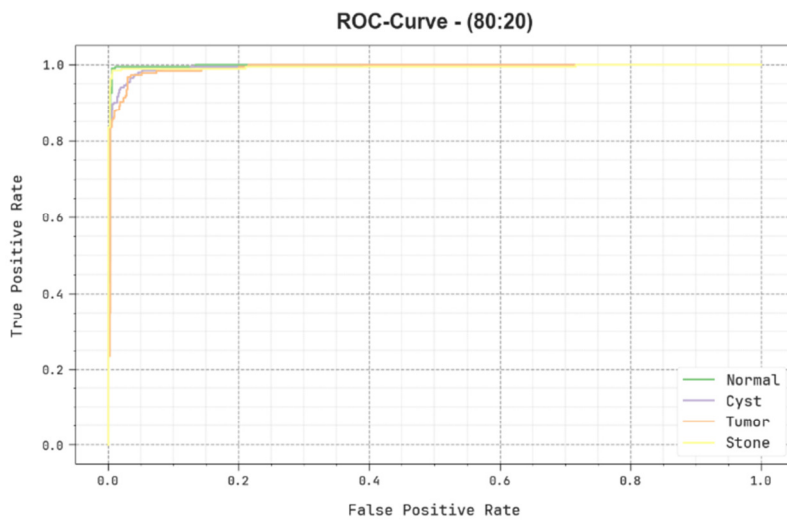


Fig. 7. ROC curve of CIDL-DSSKC in 80:20 TRPH/TSPH.

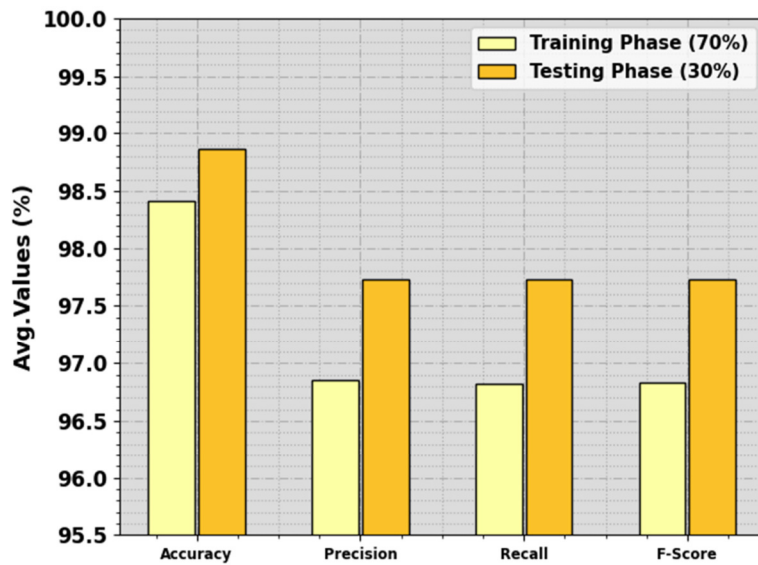


Fig. 8. Average results of CIDL-DSSKC in 70:30 TRPH/TSPH.



Fig. 9. Accuracy curve of CIDL-DSSKC in 70:30 TRPH/TSPH.



Fig. 10. Loss curve of CIDL-DSSKC in 70:30 TRPH/TSPH.

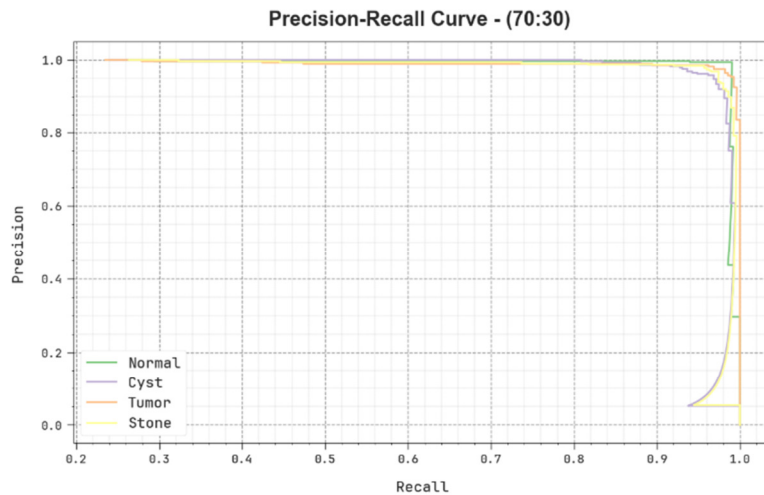


Fig. 11. Precision/Recall curve of CIDL-DSSKC in 70:30 TRPH/TSPH.

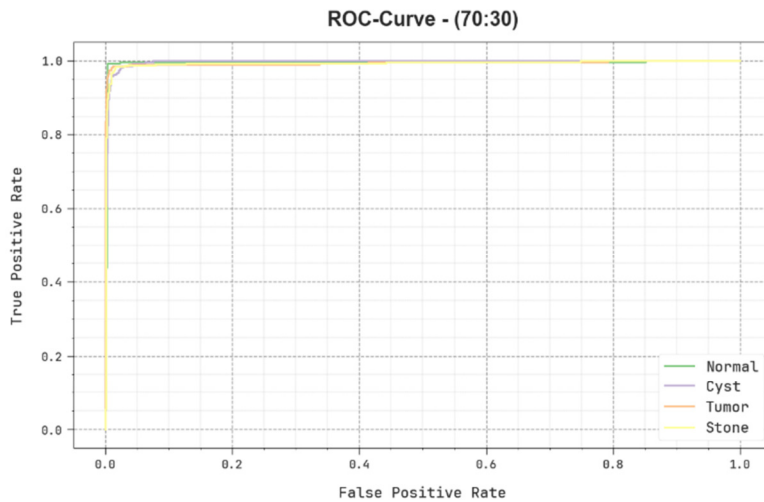


Fig. 12. ROC curve of CIDL-DSSKC on 70:30 TRPH/TSPH.

Table IV and Figure 13 compare the experimental results of CIDL-DSSKC with other methods [34]. These results show that VGG16 and Adaboost demonstrated worse outcomes, the CNN-4 model exhibited slightly better results, and the CNN-6, CNN-4, Inception v3, and 2D-CNN models offer moderately enhanced performance. However, the proposed CIDL-DSSKC technique demonstrated better results, with $accu_y$, $prec_n$, $reca_t$, and F_{score} of 98.87%, 97.73%, 97.73%, and 97.73%, respectively. Therefore, the CIDL-DSSKC can be applied for the automated detection of kidney cancer.

TABLE IV. COMPARISON WITH OTHER METHODS [34]

Models	Accuracy	Precision	Recall	F-Score
VGG16	60.00	83.62	73.55	80.11
ResNet50	96.00	92.80	93.66	94.12
CNN-6	97.00	91.76	93.91	92.06
CNN-4	92.00	92.10	93.39	90.81
InceptionV3	97.00	95.84	94.31	90.91
AdaBoost	75.00	90.44	94.12	90.49
2D-CNN	97.00	90.66	90.12	93.88
CIDL-DSSKC	98.87	97.73	97.73	97.73

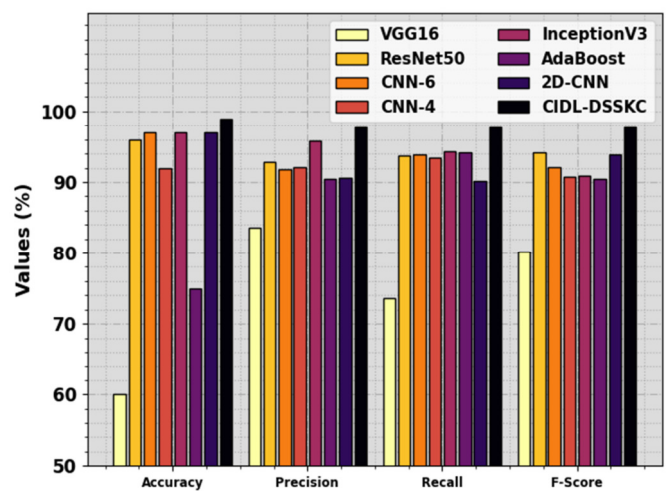


Fig. 13. Comparative results of CIDL-DSSKC with other methods.

V. CONCLUSION

This study presented the CIDL-DSSKC to detect kidney cancer in renal images, integrating Median and Wiener filters for image preprocessing, the Xception model for feature extraction, and β -VAE for classification. The experimental results in a CT kidney dataset [26] with 4000 samples in four classes (Normal, Cyst, Tumor, and Stone) demonstrated the effectiveness of the CIDL-DSSKC, as it achieved an average accuracy of 98.33%, precision of 96.65%, recall of 96.66%, and F1-score of 96.65% during training in 80% of the dataset. In the testing phase, using 20% of the dataset, the system achieved average accuracy of 97.81%, precision of 95.61%, recall of 95.54%, and F1-score of 95.56%. These results indicate that the CIDL-DSSKC can accurately and efficiently detect and classify kidney cancer types, providing radiologists with a reliable decision-support tool. The findings of this study suggest that the proposed approach not only enhances diagnostic accuracy, but also reduces the time and effort required for manual analysis, potentially improving patient outcomes. Compared to traditional methods, the proposed approach offers a more robust and automated solution for the detection of kidney cancer. Future research could further optimize the model parameters, incorporate larger and more diverse datasets, and explore integrating other advanced deep learning techniques to improve classification performance. This study lays a solid foundation for the development of more sophisticated and comprehensive diagnostic tools in the field of medical imaging.

DECLARATIONS OF INTEREST

The authors declare that they have no conflict of interest.

ACKNOWLEDGMENTS

The authors would like to acknowledge the support of Prince Sultan University, Riyadh, Saudi Arabia, in paying the Article Processing Charges (APC) of this publication. Special acknowledgment to Automated Systems and Soft Computing Lab (ASSCL), Prince Sultan University, Riyadh, Saudi Arabia.

REFERENCES

- [1] F. Hao, X. Liu, M. Li, and W. Han, "Accurate Kidney Pathological Image Classification Method Based on Deep Learning and Multi-Modal Fusion Method with Application to Membranous Nephropathy," *Life*, vol. 13, no. 2, Feb. 2023, Art. no. 399, <https://doi.org/10.3390/life13020399>.
- [2] J. Noorbakhsh *et al.*, "Deep learning-based cross-classifications reveal conserved spatial behaviors within tumor histological images," *Nature Communications*, vol. 11, no. 1, Dec. 2020, Art. no. 6367, <https://doi.org/10.1038/s41467-020-20030-5>.
- [3] E. Marostica *et al.*, "Development of a Histopathology Informatics Pipeline for Classification and Prediction of Clinical Outcomes in Subtypes of Renal Cell Carcinoma," *Clinical Cancer Research*, vol. 27, no. 10, pp. 2868–2878, May 2021, <https://doi.org/10.1158/1078-0432.CCR-20-4119>.
- [4] S. Tabibu, P. K. Vinod, and C. V. Jawahar, "Pan-Renal Cell Carcinoma classification and survival prediction from histopathology images using deep learning," *Scientific Reports*, vol. 9, no. 1, Jul. 2019, Art. no. 10509, <https://doi.org/10.1038/s41598-019-46718-3>.
- [5] E. Wulczyn *et al.*, "Deep learning-based survival prediction for multiple cancer types using histopathology images," *PLOS ONE*, vol. 15, no. 6, 2020, Art. no. e0233678, <https://doi.org/10.1371/journal.pone.0233678>.
- [6] Y. Jiao, J. Li, C. Qian, and S. Fei, "Deep learning-based tumor microenvironment analysis in colon adenocarcinoma histopathological whole-slide images," *Computer Methods and Programs in Biomedicine*, vol. 204, Jun. 2021, Art. no. 106047, <https://doi.org/10.1016/j.cmpb.2021.106047>.
- [7] H. J. Jang, A. Lee, J. Kang, I. H. Song, and S. H. Lee, "Prediction of clinically actionable genetic alterations from colorectal cancer histopathology images using deep learning," *World Journal of Gastroenterology*, vol. 26, no. 40, pp. 6207–6223, Oct. 2020, <https://doi.org/10.3748/wjg.v26.i40.6207>.
- [8] J. Kers *et al.*, "Deep learning-based classification of kidney transplant pathology: a retrospective, multicentre, proof-of-concept study," *The Lancet Digital Health*, vol. 4, no. 1, pp. e18–e26, Jan. 2022, [https://doi.org/10.1016/S2589-7500\(21\)00211-9](https://doi.org/10.1016/S2589-7500(21)00211-9).
- [9] M. H. Almusawy, "Improved Arithmetic Optimization with Deep Learning Driven Traffic Congestion Control for Intelligent Transportation Systems in Smart Cities," *Journal of Smart Internet of Things*, vol. 2022, no. 1, pp. 81–96, Dec. 2022, <https://doi.org/10.2478/jsiot-2022-0006>.
- [10] A. Sinha, P. Jha, B. Kumar, A. Mishra, V. Ujjwal, and A. Singh, "Blockchain-Based Smart Home Network Security through ML," *Journal of Smart Internet of Things*, vol. 2022, no. 1, pp. 1–9, Dec. 2022, <https://doi.org/10.2478/jsiot-2022-0001>.
- [11] W. Alkaber and F. Assiri, "Predicting the Number of Software Faults using Deep Learning," *Engineering, Technology & Applied Science Research*, vol. 14, no. 2, pp. 13222–13231, Apr. 2024, <https://doi.org/10.48084/etasr.6798>.
- [12] F. Lin *et al.*, "A CT-based deep learning model for predicting the nuclear grade of clear cell renal cell carcinoma," *European Journal of Radiology*, vol. 129, Aug. 2020, Art. no. 109079, <https://doi.org/10.1016/j.ejrad.2020.109079>.
- [13] C. Ohe *et al.*, "Deep learning-based predictions of clear and eosinophilic phenotypes in clear cell renal cell carcinoma," *Human Pathology*, vol. 131, pp. 68–78, Jan. 2023, <https://doi.org/10.1016/j.humpath.2022.11.004>.
- [14] A. A. Najm, I. K. Ibraheem, A. T. Azar, and A. J. Humaidi, "Genetic Optimization-Based Consensus Control of Multi-Agent 6-DoF UAV System," *Sensors*, vol. 20, no. 12, Jan. 2020, Art. no. 3576, <https://doi.org/10.3390/s20123576>.
- [15] E. Emary, H. M. Zawbaa, A. E. Hassanien, G. Schaefer, and A. T. Azar, "Retinal blood vessel segmentation using bee colony optimisation and pattern search," in *2014 International Joint Conference on Neural Networks (IJCNN)*, Beijing, China, Jul. 2014, pp. 1001–1006, <https://doi.org/10.1109/IJCNN.2014.6889856>.
- [16] T. Ashfaq *et al.*, "A Machine Learning and Blockchain Based Efficient Fraud Detection Mechanism," *Sensors*, vol. 22, no. 19, Jan. 2022, Art. no. 7162, <https://doi.org/10.3390/s22197162>.
- [17] A. Koubaa, A. Ammar, M. Alahdab, A. Kanhouch, and A. T. Azar, "DeepBrain: Experimental Evaluation of Cloud-Based Computation Offloading and Edge Computing in the Internet-of-Drones for Deep Learning Applications," *Sensors*, vol. 20, no. 18, Jan. 2020, Art. no. 5240, <https://doi.org/10.3390/s20185240>.
- [18] A. K. Chanchal, A. Kumar, S. Lal, and J. Kini, "Efficient and robust deep learning architecture for segmentation of kidney and breast histopathology images," *Computers & Electrical Engineering*, vol. 92, Jun. 2021, Art. no. 107177, <https://doi.org/10.1016/j.compeleceng.2021.107177>.
- [19] L. Zhou, Z. Zhang, Y.-C. Chen, Z.-Y. Zhao, X.-D. Yin, and H.-B. Jiang, "A Deep Learning-Based Radiomics Model for Differentiating Benign and Malignant Renal Tumors," *Translational Oncology*, vol. 12, no. 2, pp. 292–300, Feb. 2019, <https://doi.org/10.1016/j.tranon.2018.10.012>.
- [20] M. Zhu, B. Ren, R. Richards, M. Suriawinata, N. Tomita, and S. Hassanpour, "Development and evaluation of a deep neural network for histologic classification of renal cell carcinoma on biopsy and surgical resection slides," *Scientific Reports*, vol. 11, no. 1, Mar. 2021, Art. no. 7080, <https://doi.org/10.1038/s41598-021-86540-4>.
- [21] H. A. Abdeltawab, F. A. Khalifa, M. A. Ghazal, L. Cheng, A. S. El-Baz, and D. D. Gondim, "A deep learning framework for automated classification of histopathological kidney whole-slide images," *Journal*

- of Pathology Informatics, vol. 13, Jan. 2022, Art. no. 100093, <https://doi.org/10.1016/j.jpi.2022.100093>.
- [22] S. Schulz *et al.*, "Multimodal Deep Learning for Prognosis Prediction in Renal Cancer," *Frontiers in Oncology*, vol. 11, Nov. 2021, <https://doi.org/10.3389/fonc.2021.788740>.
- [23] K. H. Uhm *et al.*, "Deep learning for end-to-end kidney cancer diagnosis on multi-phase abdominal computed tomography," *npj Precision Oncology*, vol. 5, no. 1, pp. 1–6, Jun. 2021, <https://doi.org/10.1038/s41698-021-00195-y>.
- [24] A. A. Aatresh *et al.*, "Efficient deep learning architecture with dimension-wise pyramid pooling for nuclei segmentation of histopathology images," *Computerized Medical Imaging and Graphics*, vol. 93, Oct. 2021, Art. no. 101975, <https://doi.org/10.1016/j.compmedimag.2021.101975>.
- [25] J. DiPalma, A. A. Suriawinata, L. J. Tafe, L. Torresani, and S. Hassanpour, "Resolution-based distillation for efficient histology image classification," *Artificial Intelligence in Medicine*, vol. 119, Sep. 2021, Art. no. 102136, <https://doi.org/10.1016/j.artmed.2021.102136>.
- [26] "CT Kidney Dataset: Normal-Cyst-Tumor and Stone." <https://www.kaggle.com/datasets/nazmul0087/ct-kidney-dataset-normal-cyst-tumor-and-stone>.
- [27] C. R. Park, S. H. Kang, and Y. Lee, "Median modified wiener filter for improving the image quality of gamma camera images," *Nuclear Engineering and Technology*, vol. 52, no. 10, pp. 2328–2333, Oct. 2020, <https://doi.org/10.1016/j.net.2020.03.022>.
- [28] F. Chollet, "Xception: Deep Learning with Depthwise Separable Convolutions," in *2017 IEEE Conference on Computer Vision and Pattern Recognition (CVPR)*, Honolulu, HI, USA, Jul. 2017, pp. 1800–1807, <https://doi.org/10.1109/CVPR.2017.195>.
- [29] Z. A. Alkareem Alyasseri *et al.*, "A hybrid flower pollination with β -hill climbing algorithm for global optimization," *Journal of King Saud University - Computer and Information Sciences*, vol. 34, no. 8, Part A, pp. 4821–4835, Sep. 2022, <https://doi.org/10.1016/j.jksuci.2021.06.015>.
- [30] I. Cetin, M. Stephens, O. Camara, and M. A. González Ballester, "Attribute-based interpretable representations of medical images with variational autoencoders," *Computerized Medical Imaging and Graphics*, vol. 104, Mar. 2023, Art. no. 102158, <https://doi.org/10.1016/j.compmedimag.2022.102158>.
- [31] U. Hameed, M. Ur Rehman, A. Rehman, R. Damaševičius, A. Sattar, and T. Saba, "A deep learning approach for liver cancer detection in CT scans," *Computer Methods in Biomechanics and Biomedical Engineering: Imaging & Visualization*, vol. 11, no. 7, Jan. 2024, Art. no. 2280558, <https://doi.org/10.1080/21681163.2023.2280558>.
- [32] S. Al-Otaibi, M. Mujahid, A. R. Khan, H. Nobanee, J. Alyami, and T. Saba, "Dual Attention Convolutional AutoEncoder for Diagnosis of Alzheimer's Disorder in Patients Using Neuroimaging and MRI Features," *IEEE Access*, vol. 12, pp. 58722–58739, 2024, <https://doi.org/10.1109/ACCESS.2024.3390186>.
- [33] S. R. Waheed, N. M. Suaib, M. S. M. Rahim, A. R. Khan, S. A. Bahaj, and T. Saba, "Synergistic Integration of Transfer Learning and Deep Learning for Enhanced Object Detection in Digital Images," *IEEE Access*, vol. 12, pp. 13525–13536, 2024, <https://doi.org/10.1109/ACCESS.2024.3354706>.
- [34] D. Alzu'bi *et al.*, "Kidney Tumor Detection and Classification Based on Deep Learning Approaches: A New Dataset in CT Scans," *Journal of Healthcare Engineering*, vol. 2022, no. 1, 2022, Art. no. 3861161, <https://doi.org/10.1155/2022/3861161>.